Title: Early Hadean Earth conditions were ideal for prebiotic chemistry

Authors: L. Loth[1,2*], J. Bastias-Silva[1,2,3], C. Antoine[1,2], D. Ehrenreich[2,4], N. D. Greber[1,2,5], L. Caricchi[1,2]

Affiliations:

[1]Department of Earth Sciences, University of Geneva, Rue des Maraîchers 13, 1205 Geneva, Switzerland

[2]Centre Vie dans l'Univers, Faculté des sciences, Université de Genève, Quai Ernest-Ansermet 30, 1211 Genève 4, Switzerland

[3]Carrera de Geología, Facultad de Ingeniería, Universidad Andrés Bello, Santiago, Chile

[4]Observatoire Astronomique de l'Université de Genève, Chemin Pegasi 51, 1290 Versoix, Switzerland

[5]Muséum d'histoire naturelle de Genève, Route de Malagnou 1, 1208 Genève, Switzerland

*Corresponding author. Email: lili.loth@unige.ch

Submitting author ORCID: https://orcid.org/0009-0005-1306-2213

PREPRINT STATUS STATEMENT: Please note that this manuscript is a non-peer-reviewed preprint submitted to EarthArXiv. It is currently under peer review at Science.

Abstract: The time at which surface conditions favorable for prebiotic chemistry were established on Earth remains debated. Following magma-ocean solidification, high atmospheric pressure modulated the release of water from Earth's primary crust. Here, we model the coupled formation of early oceans and felsic crust under these conditions. Our calculations show that a hydrated primary crust forms, resulting in shallow oceans and enabling felsic magmatism. Together, this facilitated the emergence of land and established environments conducive to prebiotic chemistry, such as lakes and lagoons, rapidly after magma-ocean solidification. We propose that a planet's initial water content and the interactions between the atmosphere and geosphere governs the emergence of habitable surface environments on early Earth and, potentially, rocky exoplanets.

Main Text:

The nature of Earth's surface environment following magma ocean solidification remains poorly constrained, hampering our understanding of the conditions under which life emerged. Any model for the origin of life requires liquid water as a central element for prebiotic chemistry (*1*, *2*). Proposed environments for life's origin range from deep-water settings such as submarine hydrothermal vents (*3*, *4*) to shallow-water settings like ponds and lakes (*5*, *6*). However, deep water bodies can represent an impediment to the concentration of organic compounds necessary for the efficient production of the building blocks of life (*5*, *6*). Consequently, constraining how and when oceans and emerged land formed during Earth's first billion years is central to understanding the conditions that led to the emergence of life (*1*, *7*, *8*). In this context, an important but underexplored factor is the interaction between magmatism and the atmosphere after magma ocean solidification.

Earth's secondary atmosphere formed through the release of volatiles from the mantle during magma ocean solidification (*9*). Current models suggest that once the magma ocean solidified, the atmosphere was CO_2-rich, H_2O-poor (*10–13*) and dense, reaching pressures between 100 and 300 bar (*11*, *13*). At this stage, the mantle's water concentration is estimated to have ranged between 500 µg/g and 4000 µg/g (*10*, *14–16*), equivalent to 2 to 15 present-day ocean masses (*14*). Once the magma ocean surface cooled below its solidus, the deeper mantle remained partially molten, allowing melt extraction and eruption to form a primary crust (*17*, *18*). Because volatile solubility in magmas depends strongly on pressure (*19*, *20*), atmospheric pressures of 100 to 300 bar suppressed water degassing from erupted magmas (*17*), potentially creating a global reservoir of hydrous mafic crust. Constraining the water budget of this early crust is critical because it exerts a first-order control on the evolution of Earth's surface environment and the production of felsic crust (*21*). Crustal water content regulates the quantity of water released to the atmosphere that subsequently condenses as seawater (*17*). Furthermore, partial melting or fractionation of hydrous mafic lithologies generates buoyant felsic rocks, such as granitoids, which promote topographic relief and emergence of subaerial land (*21–23*).

Water content of the primary crust and its implication for granitoid formation

Water content of mantle-derived melts

Mantle melting is governed by the mantle geotherm and the peridotite solidus. Before the solidification of the magma ocean, the asthenospheric temperatures remained higher than the mantle solidus over a depth interval that depends on the mantle potential temperature and the water content of the mantle (*24–26*) (Fig. 1a, Fig. 1b). The presence of water enhances melt production by substantially depressing the peridotite solidus (*27*, *28*), triggering initial melting at significantly higher pressures than under dry conditions (Fig. 1c, Fig. 1d). Because H_2O behaves as a strongly incompatible element during partial melting of the mantle (*29*), it partitions preferentially into the primary mafic melt phase during early low-degree melting at depth. The ascent of these melts resulted in the transfer of water from the mantle toward the Earth's surface.

Using a Monte Carlo approach, we simulate the partial melting of the mantle and its impact on the water content of the primary crust, by sampling eight parameters (Supplementary Materials, Fig. S1, Table S1). Sensitivity tests (Fig. S2) identify two parameters that exert a primary control on the volume of mafic magma produced and its water content: (i) the initial water content of the mantle and (ii) mantle potential temperature. We therefore sample these two parameters from uniform distributions that cover the plausible range of parameters reported for early Hadean conditions, (500 to 4000 µg/g for mantle water content (*10*, *14–16*) and 1600 to 2000 K for mantle potential temperature (*24–26*). We further assume a fixed conductive lid thickness (i.e. lithosphere) of 32 km (approximately 1 GPa), corresponding to the midpoint of the 16 to 48 km (approximately 0.5 – 1.5 GPa) range proposed for the early Hadean (*30*). Materials for conductive lid thicknesses of 16 and 48 km (Fig. S3, Fig. S4) are presented in the Supplementary Information, showing that varying the lid thickness within this range does not significantly affect our results.

We calculate the thickness of the mafic crust assuming that melt is extracted from the mantle if the melt fraction is above a connectivity threshold of 0.03 (*31*). The simulations show that the depth range from which mafic melts are extracted increases with water content of the mantle and mantle potential temperature (Fig. 2a). Additionally, while the mantle potential temperature controls the thickness of the mafic crust, its water content is almost entirely controlled by the initial water content of the mantle (Fig. 2a). The volume of melt extracted from the mantle is equivalent to a global layer from 8 to 57 km thickness, with a median of 28 km (Fig. 2b, Fig. S3). Our simulations furthermore show that primary mafic mantle melts contain mostly between 0.4 and 2.3 wt.% H_2O, with more than 50% of the simulations yielding water content above 1.35 wt.% (Fig. 2c, Fig. S3). Assuming that melts ascending from the mantle retained all their water during emplacement, the primary crust could have contain up to 1.5 times the present-day ocean volume.

Granitoid formation

The result that these primary mantle melts contain a substantial amount of water has important implications for the formation of felsic lithologies like granitoids very early in Earth's history, as the key prerequisite for their generation is the presence of H_2O in the mafic melt or crust (*21*, *32*) (Fig. 3a, Fig. S4). Dissolved water alters the phase equilibria of cooling melts, by lowering its liquidus temperature and strongly suppressing the early crystallization of plagioclase relative to hydrous ferromagnesian silicates like amphibole, resulting in a relatively strong enrichment of Al_2O_3 and SiO_2 in the residual melt (*33*, *34*). Experimental studies show that fractional crystallization of mafic melts (*35*, *36*) and partial melting of mafic crust (*32*, *33*) can produce between 10 and 30 wt.% felsic melts (above 60 wt.% of SiO_2) when the parental material contains more than 0.5 wt.% H_2O (Fig. S5, (*33*, *34*)). The transformation of 10 to 30% of the primary mafic mantle melt into felsic crust produces 10 – 40% of the modern felsic crust if the mantle contains 500 µg/g H_2O and 30 – 80% if it contains 4000 µg/g H_2O (Fig. 3b, Fig. S4).

Previous models have considered the production of felsic rocks to require a water-poor mafic crust to first undergo hydrothermal alteration and enrichment in H_2O by seawater, followed by burial to pressures and temperatures sufficient for partial melting (*21*). Our calculations instead suggest that mafic melt extracted from the mantle, already contained sufficient water to form abundant felsic rocks either by fractional crystallisation or partial melting just after magma ocean solidification (Fig. 3a, Fig. 3b, Fig. S4, (*33*, *34*)). This remains the case even if mantle melts lost part of their water to the atmosphere during eruption and crust formation, as the erupting melts would have retained more than 0.7 wt.% H_2O at atmospheric pressures that were estimated to exceed 100 bar at the end of the magma ocean (*11*, *13*, *20*).

Depth of the first oceans and the likelihood for emerged land

Formation of first oceans

Once the surface conditions permit the existence of liquid water, ocean volume is controlled by the mass of H_2O extracted from the mantle by ascending melts and ultimately released to the atmosphere by magmatism (*9*, *17*). The condensation of this degassed magmatic water into liquid oceans further requires that surface temperatures are below the critical point of water under a dense CO_2 atmosphere (300 – 600 K) (*9*, *37*). The efficiency of the transfer of H_2O from the crust to the atmosphere depends on the modality of magma emplacement and atmospheric pressure. In a scenario where crust forms through the progressive accumulation of surface lava flows (e.g., a heat-pipe Earth; (*38*)), high atmospheric pressure suppresses water release from the magma because of the dependence of water solubility on pressure (*11*, *13*). Thus, basalts cooling at the surface would have retained up to 1.2 wt.% and 0.7 wt.% H_2O for atmospheric pressures of 300 bar and 100 bar, respectively (*20*). On the other hand, magma emplaced at depth undergoes crystallization-induced degassing (*39*, *40*), which would have maximised H_2O release during solidification. Under these conditions, H_2O is chiefly released to the atmosphere with only minor amounts retained in hydrous mineral phases (e.g., hornblende).

Using the calculated volume and water content of the residual melts extracted from the mantle (Supplementary Materials, Fig. 2, Fig. 3a), we compute the global equivalent volume of surface water that could form under three end-member emplacement scenarios: (i) all melt erupts at the surface under atmospheric pressures of 100 bar; (ii) 300 bar ("heat-pipe Earth"), and (iii) all melt is emplaced and crystallizes at depth ("all-intrusive"). Conservatively, for this last case, we consider that the water bearing mineral hornblende makes up 10 wt.% of the solidified mineral assembly (*34*, *41*).

Considering the wide range of conditions explored by our Monte Carlo simulations, including variations in initial mantle H_2O content, mantle potential temperature, atmospheric pressure, and melt emplacement mode (eruption at the surface versus crystallization at depth), we find that most simulations produce less than 50% of the modern ocean volume (Fig. 3c, Fig. 3d, Fig. S6). When mantle melts erupt at the surface (heat-pipe Earth scenarios), the median value of the surface water volume is 16% and 2% of modern ocean volumes, corresponding to ocean depths of about 450 meters and 60 meters (Fig. 3d, Fig. S7) for atmospheric pressure of 100 and 300 bars, respectively. In contrast, melt crystallization at depth within the crust (all-intrusive scenarios) allows for larger surface water volumes. Across the explored parameter space, the amount of surface water exceeds 50% of the present-day ocean volume for initial mantle H_2O contents above around 0.22 wt.% (Fig. 3c, Fig. S6). Importantly, our results for the "all-intrusive" scenario provide maximum estimates of the water that can be released to the atmosphere because previous studies considering a wider range of parameters suggest that magma emplaced at depth can retain more water than assumed in our model (*40*).

Implications for emerged lands and prebiotic chemistry

Whether land emerges under these water inventories depends on the topographic relief of the primary crust. Isostatic calculations for early Earth conditions indicate that a purely mafic crust could sustain ~1000 m of topographic relief, which increases up to 5000 m in the presence of larger amounts of felsic crust (*22*). This increased relief stems from the density contrast between the felsic blocks (2650 – 2700 kg/m^3)(*42*) and the surrounding mafic crust (3000 kg/m^3)(*42*). The low-density felsic nuclei resist gravitational recycling and can thus become locally concentrated in the upper crust, which increases regional isostatic elevation and promotes the emergence of landmasses above sea level. Furthermore, where simulated primary mafic crustal thicknesses exceed 30 km, the deepest crustal levels would undergo high-pressure phase transformations into dense (3400 kg/m^3) garnet amphibolite or eclogite (*42*, *43*). Lower-crustal delamination or drip recycling of these dense residues back into the mantle would selectively preserve the less dense, felsic-to-intermediate upper crust, further enhancing the topographic relief.

Therefore, our results show that the likelihood of emerged land following magma ocean solidification does not depend strongly on the formation processes of the primary crust. If the primary crust formed predominantly through volcanism, the relatively low ocean volume we calculate, corresponding to a surface water layer less than 1000 meters deep, implies that emerged land would have developed with high probability shortly after magma ocean solidification (Fig. 3d). In the "all-intrusive" scenario, as the volume of surface water and the volume of felsic crust are both positively correlated with the initial water content of the mantle, our results suggest that deeper oceans go together with more felsic crust (Fig. 3b, Fig. 3c). Therefore, the increase in crustal relief associated with the presence of voluminous felsic rocks allows emerged land to persist even with higher surface water volumes (*22*). Overall, our results indicate that emerged land was likely present just after the solidification of the magma ocean.

A corollary of our results is that most of our simulations produce surface water volumes that are lower than the modern surface water inventory (Fig. 3c, Fig. 3d). This implies either external addition of water since the Hadean or progressive mantle degassing to reach the modern surface water volumes. Recent H and N isotopic mass-balance calculations suggest that late-accreted external material, such as Ivuna-type carbonaceous chondrites, contributed less than 15% of Earth's surface water inventory (*16*). This implies that progressive transfer of water from the mantle to the surface was likely the dominant mechanism driving an increase in ocean volume over time. This transfer may have accelerated as atmospheric CO_2 concentrations, and thus atmospheric pressure declined through silicate weathering, allowing more water to degas from mantle-derived magmas. The drawdown of CO_2 could have thus established a positive feedback loop: early subaerial exposure of felsic and mafic crust accelerates silicate weathering, which traps atmospheric CO_2 into carbonates (*44*). The resulting drop in total atmospheric pressure progressively lowers the solubility threshold for magmatic water in subsequent volcanic pulses (*17*, *19*), enabling more water to degas and increasing ocean depth. Whether this led to a sufficient increase in ocean volume to submerge at one point the existing land or not is debated (*45*, *46*). However, it has been shown that reducing atmospheric CO_2 from 200 to 100 bar likely took more than 100 Myr (*17*). Thus, shallow oceans and emerged land persisted long after magma ocean solidification, providing an environment that enabled wetting-drying cycles in shallow water bodies, which are thought to be essential for polymerization of pre-biotic molecules (*5*, *6*, *47*).

This approach can be transferred to explore the potential of exoplanets to harbor favorable conditions for prebiotic chemistry as the volatile content of telluric planets is progressively becoming accessible through the observations of their atmospheres when transiting their stars (*48*). The water content of telluric exoplanets and slightly larger objects known as "sub-Neptunes" is an intense area of studies (*49*). Volatile species could be directly detected through the study of the outgassing atmosphere from the surface magma oceans of hot rocky planets (*50*) or the primordial gas envelopes of temperate rocky worlds (*51*). These distant planets could thus ultimately provide precious comparative cases helping us put Earth in perspective and understanding its evolution toward habitable conditions.

More broadly, our findings highlight the importance of the initial volatile inventory of planets and early atmospheric evolution in regulating the presence of surface water and, consequently, the emergence of habitable environments. Therefore, a planet primordial volatile budget and the continuous exchange between its early atmosphere and its solid interior may serve as the first-order control that ultimately sets telluric worlds on the pathway toward habitability.

References and Notes

1. B. K. D. Pearce, R. E. Pudritz, D. A. Semenov, T. K. Henning, Origin of the RNA world: The fate of nucleobases in warm little ponds. *Proc. Natl. Acad. Sci.* **114**, 11327–11332 (2017).

2. S. A. Benner, E. A. Bell, E. Biondi, R. Brasser, T. Carell, H. Kim, S. J. Mojzsis, A. Omran, M. A. Pasek, D. Trail, When Did Life Likely Emerge on Earth in an RNA-First Process? *ChemSystemsChem* **2**, e1900035 (2020).

3. J. A. Baross, S. E. Hoffman, Submarine hydrothermal vents and associated gradient environments as sites for the origin and evolution of life. *Orig. Life Evol. Biosph.* **15**, 327–345 (1985).

4. W. Martin, J. Baross, D. Kelley, M. J. Russell, Hydrothermal vents and the origin of life. *Nat. Rev. Microbiol.* **6**, 805–814 (2008).

5. B. Damer, D. Deamer, The Hot Spring Hypothesis for an Origin of Life. *Astrobiology* **20**, 429–452 (2020).

6. D. D. Sasselov, J. P. Grotzinger, J. D. Sutherland, The origin of life as a planetary phenomenon. *Sci. Adv.* **6**, eaax3419 (2020).

7. A. L. Zerkle, Biogeodynamics: bridging the gap between surface and deep Earth processes. *Philos. Trans. R. Soc. Math. Phys. Eng. Sci.* **376**, 20170401 (2018).

8. J. D. Toner, D. C. Catling, A carbonate-rich lake solution to the phosphate problem of the origin of life. *Proc. Natl. Acad. Sci.* **117**, 883–888 (2020).

9. K. Zahnle, L. Schaefer, B. Fegley, Earth's Earliest Atmospheres. *Cold Spring Harb. Perspect. Biol.* **2**, a004895–a004895 (2010).

10. L. T. Elkins-Tanton, Linked magma ocean solidification and atmospheric growth for Earth and Mars. *Earth Planet. Sci. Lett.* **271**, 181–191 (2008).

11. P. A. Sossi, A. D. Burnham, J. Badro, A. Lanzirotti, M. Newville, H. St. C. O'Neill, Redox state of Earth's magma ocean and its Venus-like early atmosphere. *Sci. Adv.* **6**, eabd1387 (2020).

12. N. V. Solomatova, R. Caracas, Buoyancy and Structure of Volatile-Rich Silicate Melts. *J. Geophys. Res. Solid Earth* **126**, e2020JB021045 (2021).

13. F. Gaillard, F. Bernadou, M. Roskosz, M. A. Bouhifd, Y. Marrocchi, G. Iacono-Marziano, M. Moreira, B. Scaillet, G. Rogerie, Redox controls during magma ocean degassing. *Earth Planet. Sci. Lett.* **577**, 117255 (2022).

14. B. Marty, The origins and concentrations of water, carbon, nitrogen and noble gases on Earth. *Earth Planet. Sci. Lett.* **313–314**, 56–66 (2012).

15. A. H. Peslier, M. Schönbächler, H. Busemann, S.-I. Karato, Water in the Earth's Interior: Distribution and Origin. *Space Sci. Rev.* **212**, 743–810 (2017).

16. L. Piani, Y. Marrocchi, T. Rigaudier, L. G. Vacher, D. Thomassin, B. Marty, Earth's water may have been inherited from material similar to enstatite chondrite meteorites. *Science* **369**, 1110–1113 (2020).

17. Y. Miyazaki, J. Korenaga, A wet heterogeneous mantle creates a habitable world in the Hadean. *Nature* **603**, 86–90 (2022).

18. S. Turner, B. Wood, T. Johnson, C. O'Neill, B. Bourdon, Formation and composition of Earth's Hadean protocrust. *Nature* **640**, 390–394 (2025).

19. P. Papale, R. Moretti, D. Barbato, The compositional dependence of the saturation surface of H2O+CO2 fluids in silicate melts. *Chem. Geol.* **229**, 78–95 (2006).

20. G. Iacono-Marziano, Y. Morizet, E. Le Trong, F. Gaillard, New experimental data and semi-empirical parameterization of H2O–CO2 solubility in mafic melts. *Geochim. Cosmochim. Acta* **97**, 1–23 (2012).

21. J.-F. Moyen, H. Martin, Forty years of TTG research. *Lithos* **148**, 312–336 (2012).

22. M. Tang, H. Chen, C.-T. A. Lee, W. Cao, Subaerial crust emergence hindered by phase-driven lower crust densification on early Earth. *Sci. Adv.* **10**, eadq1952 (2024).

23. P. Chowdhury, P. A. Cawood, J. A. Mulder, Subaerial Emergence of Continents on Archean Earth. *Annu. Rev. Earth Planet. Sci.* **53**, 443–478 (2025).

24. C. Herzberg, K. Condie, J. Korenaga, Thermal history of the Earth and its petrological expression. *Earth Planet. Sci. Lett.* **292**, 79–88 (2010).

25. J. Korenaga, Initiation and Evolution of Plate Tectonics on Earth: Theories and Observations. *Annu. Rev. Earth Planet. Sci.* **41**, 117–151 (2013).

26. D. Andrault, G. Pesce, G. Manthilake, J. Monteux, N. Bolfan-Casanova, J. Chantel, D. Novella, N. Guignot, A. King, J.-P. Itié, L. Hennet, Deep and persistent melt layer in the Archaean mantle. *Nat. Geosci.* **11**, 139–143 (2018).

27. R. F. Katz, M. Spiegelman, C. H. Langmuir, A new parameterization of hydrous mantle melting. *Geochem. Geophys. Geosystems* **4**, 2002GC000433 (2003).

28. M. M. Hirschmann, Water, melting, and the deep Earth H_2O cycle. *Annu. Rev. Earth Planet. Sci.* **34**, 629–653 (2006).

29. C. Aubaud, E. H. Hauri, M. M. Hirschmann, Hydrogen partition coefficients between nominally anhydrous minerals and basaltic melts. *Geophys. Res. Lett.* **31**, 2004GL021341 (2004).

30. S. Marchi, A. M. Alexander, R. Citron, B. C. Johnson, Impact-Generated Mixing, Melting and Vaporization of the Early Earth's Crust. *Earth Space Sci.* **13**, e2025EA004364 (2026).

31. K. Vogt, T. V. Gerya, A. Castro, Crustal growth at active continental margins: Numerical modeling. *Phys. Earth Planet. Inter.* **192–193**, 1–20 (2012).

32. J. S. Beard, G. E. Lofgren, Dehydration Melting and Water-Saturated Melting of Basaltic and Andesitic Greenstones and Amphibolites at 1, 3, and 6. 9 kb. *J. Petrol.* **32**, 365–401 (1991).

33. T. W. Sisson, T. L. Grove, Experimental investigations of the role of H20 in calc-alkaline differentiation and subduction zone magmatism.

34. O. Müntener, P. B. Kelemen, T. L. Grove, The role of H2O during crystallization of primitive arc magmas under uppermost mantle conditions and genesis of igneous pyroxenites: an experimental study. *Contrib. Mineral. Petrol.* **141**, 643–658 (2001).

35. S. Villiger, The Liquid Line of Descent of Anhydrous, Mantle-Derived, Tholeiitic Liquids by Fractional and Equilibrium Crystallization--an Experimental Study at 1{middle dot}0 GPa. *J. Petrol.* **45**, 2369–2388 (2004).

36. O. Müntener, P. Ulmer, Arc crust formation and differentiation constrained by experimental petrology. *Am. J. Sci.* **318**, 64–89 (2018).

37. N. H. Sleep, K. Zahnle, Carbon dioxide cycling and implications for climate on ancient Earth. *J. Geophys. Res. Planets* **106**, 1373–1399 (2001).

38. W. B. Moore, A. A. G. Webb, Heat-pipe Earth. *Nature* **501**, 501–505 (2013).

39. T. W. Sisson, C. R. Bacon, Gas-driven filter pressing in magmas. *Geology* **27**, 613 (1999).

40. S. Vulpius, L. Noack, Intrusive Magmatism Strongly Contributed to the Volatile Release Into the Atmosphere of Early Earth. *Geochem. Geophys. Geosystems* **23**, e2021GC010230 (2022).

41. F. Marxer, P. Ulmer, Crystallisation and zircon saturation of calc-alkaline tonalite from the Adamello Batholith at upper crustal conditions: an experimental study. *Contrib. Mineral. Petrol.* **174**, 84 (2019).

42. R. L. Rudnick, S. Gao, "Composition of the Continental Crust" in *Treatise on Geochemistry* (Elsevier, 2003; https://linkinghub.elsevier.com/retrieve/pii/B0080437516030164), pp. 1–64.

43. T. E. Zegers, P. E. Van Keken, Middle Archean continent formation by crustal delamination. *Geology* **29**, 1083 (2001).

44. J. C. G. Walker, P. B. Hays, J. F. Kasting, A negative feedback mechanism for the long-term stabilization of Earth's surface temperature. *J. Geophys. Res. Oceans* **86**, 9776–9782 (1981).

45. J. Korenaga, Was There Land on the Early Earth? *Life* **11**, 1142 (2021).

46. D. S. Abbot, N. B. Cowan, F. J. Ciesla, Indication of insensitivity of planetary weathering behavior and habitable zone to surface land fraction. *Astrophys. J.* **756**, 178 (2012).

47. S. Becker, J. Feldmann, S. Wiedemann, H. Okamura, C. Schneider, K. Iwan, A. Crisp, M. Rossa, T. Amatov, T. Carell, Unified prebiotically plausible synthesis of pyrimidine and purine RNA ribonucleotides. *Science* **366**, 76–82 (2019).

48. R. Wordsworth, L. Kreidberg, Atmospheres of Rocky Exoplanets. *Annu. Rev. Astron. Astrophys.* **60**, 159–201 (2022).

49. R. Hu, A. Bello-Arufe, A. Tokadjian, J. Yang, M. Damiano, P.-A. Roy, L.-P. Coulombe, N. Madhusudhan, S. Constantinou, B. Benneke, A water-rich interior in the temperate sub-Neptune K2-18 b revealed by JWST. arXiv [Preprint] (2025). https://doi.org/10.48550/ARXIV.2507.12622.

50. A. Bello-Arufe, M. Damiano, K. A. Bennett, R. Hu, L. Welbanks, R. J. MacDonald, D. Z. Seligman, D. K. Sing, A. Tokadjian, A. V. Oza, J. Yang, Evidence for a Volcanic Atmosphere on the Sub-Earth L 98-59 b. *Astrophys. J. Lett.* **980**, L26 (2025).

51. C. Cherubim, S. Vissapragada, T. Cunningham, A. G. Meech, D. Charbonneau, R. Wordsworth, A. Householder, J. Teske, L. A. Dos Santos, N. L. Wallack, W. Misener, Z. Lin, A. McWilliam, M. Zhang, J. A. Dittmann, M. López-Morales, Helium escaping from the atmosphere of a nearby rocky exoplanet orbiting in a habitable zone. *Science* **393**, 998–1001 (2026).

52. J. Krissansen-Totton, G. N. Arney, D. C. Catling, Constraining the climate and ocean pH of the early Earth with a geological carbon cycle model. *Proc. Natl. Acad. Sci.* **115**, 4105–4110 (2018).

53. D. Turcotte, G. Schubert, *Geodynamics:* (Cambridge University Press, ed. 3, 2014; https://www.cambridge.org/core/product/identifier/9780511843877/type/book).

54. T. Katsura, A. Yoneda, D. Yamazaki, T. Yoshino, E. Ito, Adiabatic temperature profile in the mantle. *Phys. Earth Planet. Inter.* **183**, 212–218 (2010).

55. M. Charette, W. Smith, The Volume of Earth's Ocean. *Oceanography* **23**, 112–114 (2010).

Acknowledgments:

Funding: Swiss National Science Foundation (SNSF) (grant 215095)

Author contributions:

Conceptualization: LL, JBS, CA, NDG, LC

Methodology: LL, JBS

Modeling: LL

Investigation: LL, JBS, CA, NDG, LC

Visualization: LL, JBS, CA, NDG, LC

Funding acquisition: NDG, LC, DE

Project administration: NDG, LC

Supervision: NDG, LC

Writing – original draft: LL, NDG, LC

Writing – review & editing: LL, JBS, CA, NDG, LC, DE

Diversity, equity, ethics, and inclusion: This research was conducted within an international and collaborative environment at the University of Geneva. We are committed to fostering an inclusive, equitable, and diverse research community that promotes open-science practices and supports early-career researchers.

Competing interests: Authors declare that they have no competing interests.

Data, code, and materials availability: Code developed is hosted in a public repository at https://github.com/lililoth/Hadean-mantle-melting. A DOI-minted archive of the exact code version used in this study will be made available upon acceptance. All input parameters and simulation outputs are included in the manuscript and Supplementary Materials.

Supplementary Materials

Materials and Methods

Figs. S1 to S8

Table S1

References (*1* – *55*)

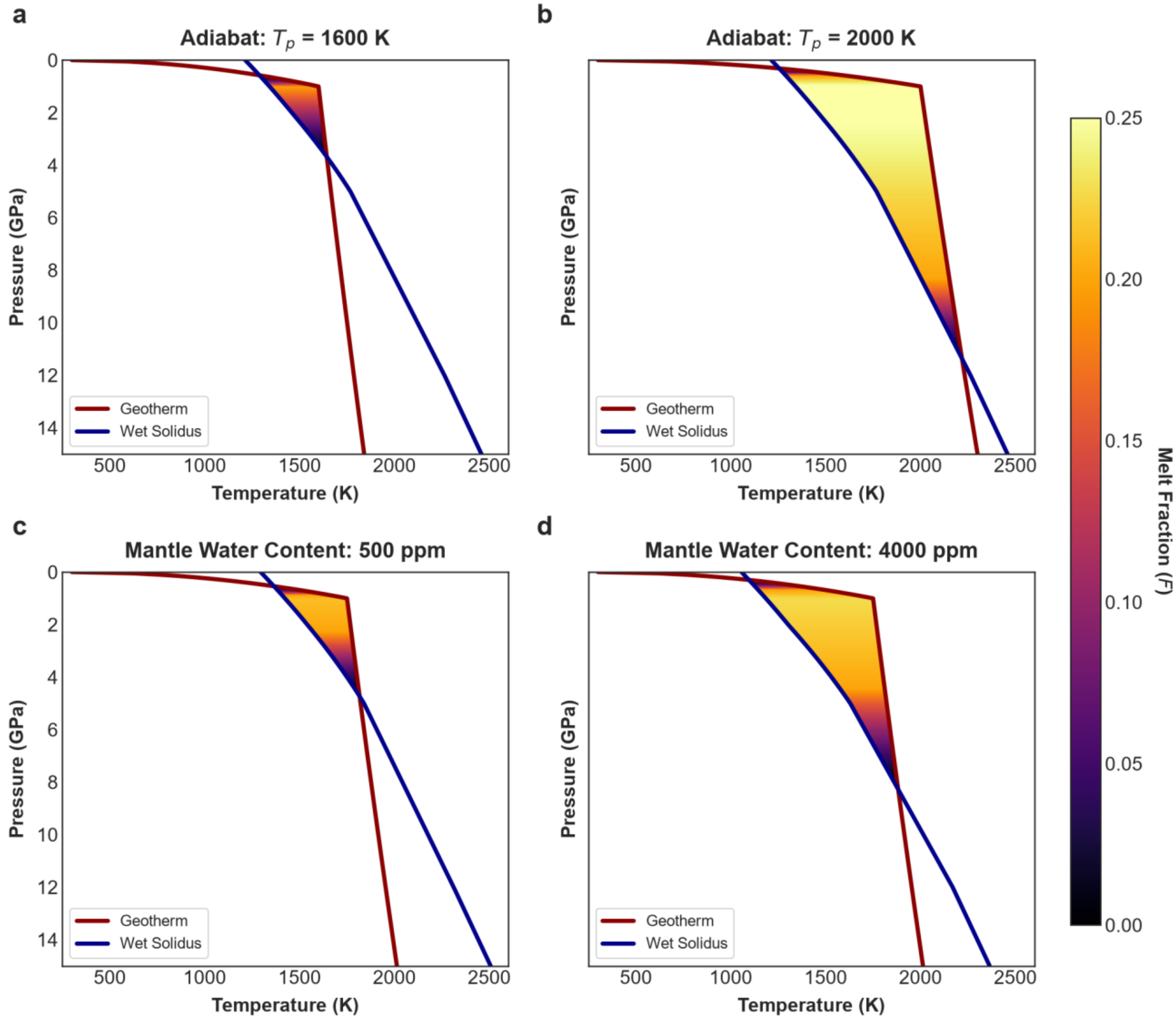

Fig. 1. Pressure–temperature thermodynamic diagrams mapping the intersection of the Hadean mantle geotherm and the wet solidus across varied parameter spaces. Red curves are calculated mantle geotherm profiles. Blue curves are wet solidus. Panels (a) and (b) illustrate the impact of mantle potential temperature (Tp) on the geotherm slope and the resulting melt fraction (F). Panels (c) and (d) demonstrate the effect of variable initial mantle water content. Complete

thermodynamic equations and parameters are provided in Methods (Supplementary Materials) and Table S1.

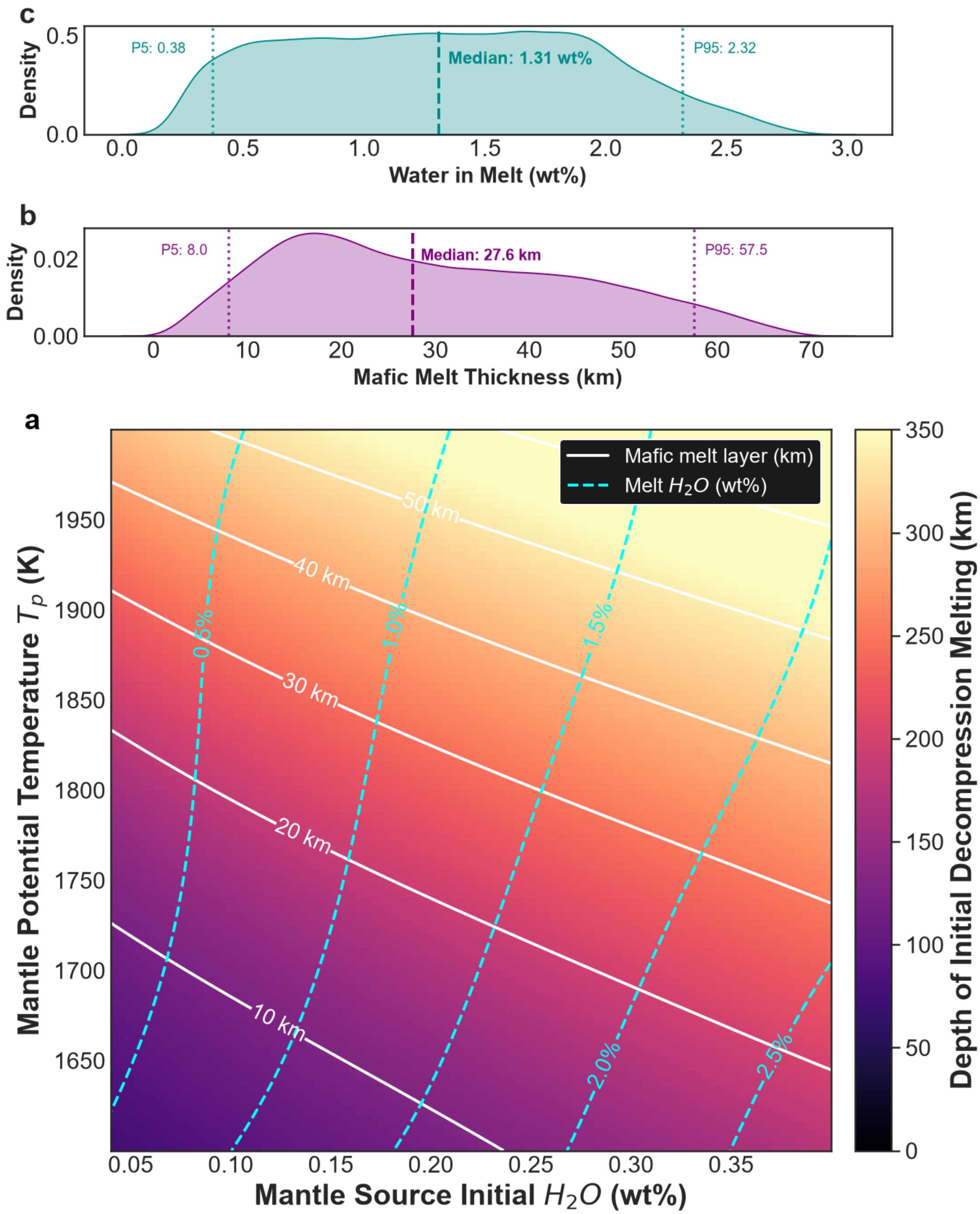

Fig. 2. Monte Carlo simulation outputs. Panel (a): Predictive petrological abacus mapping partial melting behavior as a function of mantle source initial H_2O content (x-axis) and mantle

potential temperature (Tp; y-axis) at a lithospheric pressure boundary of 1 GPa. Results for lithospheric pressures of 0.5 and 1.5 GPa are shown in Fig. S3. The background color gradient denotes the maximum depth of melting (km). White solid contours delineate the calculated thickness of the extracted mafic melt layer (in km; a proxy for mafic crustal thickness), while cyan dashed contours indicate the resulting water concentration within the generated melt (wt.%). Thermodynamic melting parameterizations are adapted from ref. (27) and calibrated for Hadean mantle conditions (Supplementary Materials). Panels (b) and (c): Kernel density estimation (KDE) plots illustrating the overall probability distributions, median values (dashed lines) and 90% confidence intervals (dotted lines) for the thickness of the primary crust (b); and its bulk H_2O concentration (c), extracted across the entire suite of Monte Carlo simulation runs.

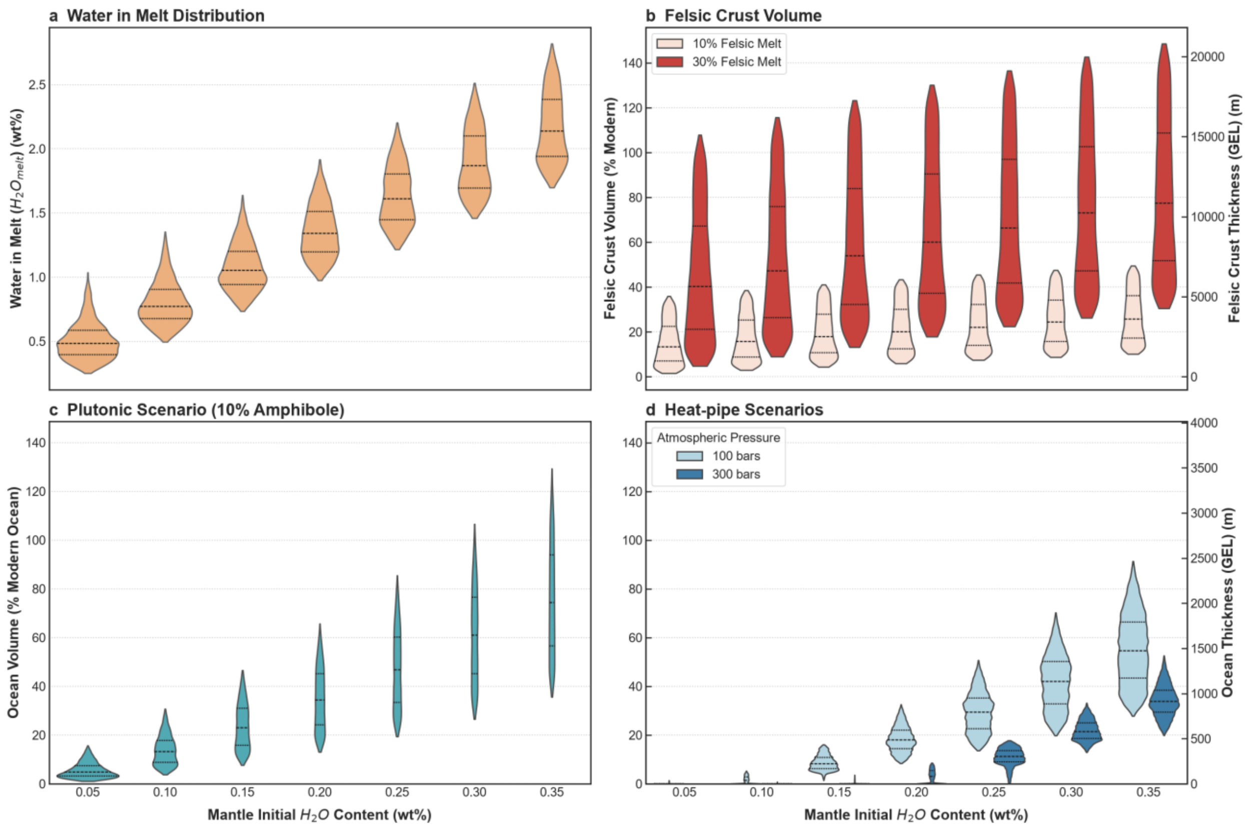

Fig. 3. Water content of mafic melts, felsic crust production and ocean volumes as function of mantle initial water content. Violin plots illustrate probability distributions from Monte Carlo simulations; dashed lines indicate the median and the 25th and 75th percentiles. Results are shown for a lithospheric lid pressure of 1.0 GPa, those for 0.5 and 1.5 GPa are given in Fig. S4. Panel (a): Water content of primary mafic melts extracted from the mantle as a function of initial mantle water content (500 – 4000 µg/g). Panel (b): Generated felsic crust volume expressed as a percentage of modern continental crust volume (% Modern Continental Crust; left axis) and equivalent global layer thickness (GEL, meters; right axis). Light pink violins represent a conversion efficiency of 10% felsic melt production, whereas dark red violins represent a 30% yield. Panel (c): Calculated Ocean volume (% Modern Ocean; left axis) and equivalent global layer ocean thickness (GEL, meters; right axis) under an all-intrusive (plutonic) scenario where melts crystallize in the crust, assuming 10 wt.% residual amphibole retention. Panel (d): Calculated Ocean volume (% Modern Ocean; left axis) and equivalent global layer ocean thickness (GEL,

meters; right axis) under a heat-pipe scenario where all melts erupt at the surface under a 100 or 300 bar atmospheric pressure.

Supplementary Materials for

Early Hadean Earth conditions were ideal for prebiotic chemistry

L. Loth, J. Bastias-Silva, C. Antoine, D. Ehrenreich, N. D. Greber, L. Caricchi
Corresponding author: lili.loth@unige.ch

The PDF file includes:

Materials and Methods
Figs. S1 to S8
Table S1

Materials and Methods

Parametrization of Hadean mantle melting

To evaluate the generation of the primary basaltic crust, we simulate partial melting of a primitive, volatile-rich Hadean mantle. Melting of this primitive mantle was parametrized following the method and equation of ref. (*27*), which describes melt fraction as a function of pressure, temperature and bulk water content.

Melting occurs where the geotherm exceeds the solidus temperature. To account for the extreme thermal regime of the early Earth following magma ocean crystallization, the geotherm (T_{geo}) is parameterized under high-temperature Hadean conditions (*26*) using the mantle potential temperature (T_P = 1600 – 2000 K; (*24 – 26*)), surface temperature (T_{surf} = 300 K; (*52*)), and pressure at the base of the lithosphere (P_{lith}) of 0.5 to 1.5 GPa (*30*). Within the shallow conductive lithosphere ($P < P_{lith}$), temperature increases rapidly via non-linear scaling across a thin lid anchored to T_{surf} (*53*). Beneath the lithosphere ($P > P_{lith}$), the profile transitions into a hot, convective mantle adiabat governed by T_P and the adiabatic gradient parameter α (*54*):

$$(1) \quad T_{geo}(P) = \begin{cases} T_{surf} + \left(T_p - T_{surf}\right)\sqrt{\dfrac{P}{P_{lith}}}, & \text{for } P \leq P_{lith} \\ T_p \exp[\alpha \cdot (P - P_{lith})], & \text{for } P > P_{lith} \end{cases}$$

Where P is pressure in GPa and temperatures are in Kelvin. We parametrize the baseline solidus temperature for a rigid, pristine dry peridotite mantle (T_s^{dry}) across two distinct pressure regimes to account for high-pressure phase transitions and mineral compressibility (*27*):

$$(2) \quad T_s^{dry}(P) = \begin{cases} (1085 + 132.9P - 5.1P^2) + 273.15, & \text{for } P < 5.0 \text{ GPa} \\ \left(1622 + 65(P - 5.0)\right) + 273.15, & \text{for } P \geq 5.0 \text{ GPa} \end{cases}$$

The presence of dissolved water in the mantle depresses the peridotite solidus (*27*). The effective reduction in the solidus temperature (ΔT_s) driven by the initial mantle volatile concentration (X_{H2O}) is governed by a non-linear power law capped at a maximum depression parameter (K; (*27*)):

$$(3) \quad \Delta T_s = K \cdot X_{H_2O}{}^{0.75}$$

As the partial melts are extracted, the remaining mantle residue becomes progressively more refractory (depleted in incompatible and volatiles). To account for progressive mantle depletion during melt extraction, the effective solidus temperature (T_s^{eff}) is shifted upward as a function of cumulative extracted melt fraction ($F_{cumulative}$), regulated by the depletion coefficient γ (γ = 200 – 400 K; (*27*)):

$$(4) \quad T_s^{eff}\left(P, X_{H_2O}, F_{cumulative}\right) = T_s^{dry}(P) - \Delta T_s + \gamma \cdot F_{cumulative}$$

The melt fraction (F_i) generated at any localized pressure step (P_i) is controlled by the thermal excess above the solidus relative to the liquidus, parametrized by a power law exponent β (27):

$$(5)\quad F_i = \begin{cases} \left(\dfrac{T_{geo}(P_i) - T_s^{eff}(P_i)}{T_l(P_i) - T_s^{eff}(P_i)}\right)^{\beta}, & \text{for } T_{geo}(P_i) > T_{s,\,eff}(P_i) \\ 0, & \text{for } T_{geo}(P_i) \le T_{s,\,eff}(P_i) \end{cases}$$

where $T_{geo}(P_i)$ is the local mantle geotherm, $T_s^{eff}(P_i)$ is the effective wet solidus temperature, and $T_l(P_i)$ is the peridotite liquidus temperature at pressure P_i.

The total column thickness of primary mafic crust (h_{mafic}) generated per simulation iteration is calculated by integrating the melt fraction over depth, considering a melt extraction threshold ($F_{extract}$ = 0.03; (*30*)):

$$(6)\quad h_{mafic} = \int \max(F(z) - F_{extract},\ 0)\, dz$$

The mean water concentration of the primary mafic melt phase (X_{melt}, in wt.%) is calculated by integrating over pressure, assuming a constant mineral-melt partition coefficient for water D_{H_2O} = 0.01; (*29*)):

$$(7)\quad X_{melt} = \frac{1}{\int F\, dP} \int \left[\left(\frac{X_{H_2O}}{F(P) + D_{H_2O}(1 - F(P))}\right) \cdot F\right] dP$$

where X_{H_2O} is the initial bulk mantle water content of the mantle, and F(P) the melt fraction at a pressure P.

Monte Carlo simulations

To explore the range of plausible Hadean conditions, Monte Carlo simulations were performed over key parameters, including mantle potential temperature (Tp; 1600 – 2000 K, (*24 – 26*), bulk mantle water content, lithosphere thickness (500 – 4000 µg/g, (*10, 14 – 16*), melt productivity exponent (β), water partition coefficient (D_{H2O}), adiabatic gradient (α), melt extraction threshold and coefficient of depletion feedback (γ) (Table S1). A total of 100,000 simulations were performed to generate statistical distributions of melt fraction, melt column thickness and melt water content (Fig. S1). Global sensitivity analysis was conducted using correlation metrics to identify the dominant controlling parameters (Fig. S2). Mantle potential temperature and bulk water content exert primary control on melt productivity and melt hydration. Based on these results, simplified predictive diagrams (abacus) showing melt column thickness, melt hydration and depth of initial melting were constructed as a function mantle potential temperature and bulk water content for lithospheric pressures of 1 GPa (Fig. 2), as well as 0.5 and 1.5 GPa (Fig. S3) with all other parameters fixed at representative values (Table S1).

Felsic Crust Volumes

To estimate the generation of felsic crust via partial melting of the hydrous mafic crust or differentiation of the mafic mantle melt, we parametrize the felsic crust thickness (h_{felsic}, GEL) as a function of mafic crust thickness (h_{mafic}) and fractional conversion efficiency (ϵ_{fc}):

$$(12)\quad h_{felsic} = h_{mafic} \cdot \epsilon_{fc}$$

where h_{mafic} is the mafic melt layer (see equation 6) and ϵ_{fc} provides the fraction of felsic melt that can be obtained by partial melting or differentiation of the mafic melt. ϵ_{fc} was varied between a minimum of 0.10 and a maximum of 0.3 (Fig. S5, 33, 34).

To convert layer thicknesses into a volume expressed as a percentage of modern felsic crust, the calculated thickness is integrated over Earth's surface area (S_{Earth}):

$$(13)\quad \text{Felsic Crust Volume (\% Modern)} = \left(\frac{h_{felsic} \cdot S_{Earth}}{V_{felsic,\ modern}}\right) \times 100$$

where $V_{felsic,modern} = 7.20 \cdot 10^9$ km^3 and $S_{Earth} = 5.10 \cdot 10^8$ km^2.

Ocean Volumes

The absolute volume of water available to build early oceans is calculated by tracking volatile extraction during mantle melting and subsequent outgassing. To convert the mass fraction of water dissolved in the parental melt into a physical water layer, we use the thickness of mafic melt (or primary mafic crust) and its water content:

$$(8)\quad h_{water} = h_{mafic} \cdot \left(\frac{X_{melt}}{100}\right) \cdot \left(\frac{\rho_{crust}}{\rho_{water}}\right) = h_{mafic} \cdot X_{melt} \cdot \mathcal{C}$$

where $\mathcal{C}$ is the scaling factor, ρ_{crust} is the density of the primary mafic crust (3000 kg/m^3) and ρ_{water} is the density of liquid water (1000 kg/m^3). This scaling tracks the Global Equivalent Layer (GEL) surface water height (h_{water}) if the magmatic water mass was fully degassed at the surface.

Water extraction is dependent on the emplacement scenario of the mafic melt, i.e., either extrusive or intrusive (melt crystallized at depth). Under a purely extrusive regime (e.g., a heat-pipe Earth; (*38*)), melts erupt at the surface, trapping water in the erupted glass. The atmospheric pressure exerts a primary control on how much water can be dissolved in the melt. This saturation threshold under a high atmospheric pressure is defined as $X_{sat} = 0.071 \cdot \sqrt{P_{atm}}$; i.e., 0.71 wt.% and 1.23 wt.% of H_2O under a 100 and 300 bar atmosphere respectively (*11, 13*). The GEL height of water degassed under the heat-pipe Earth scenario ($h_{water,\ heat\text{-}pipe}$) is then a function of the water that is dissolved in the melt and the saturation threshold:

$$(9)\quad h_{water,\ heat\text{-}pipe} = \max(0, X_{melt} - X_{sat}) \cdot h_{mafic} \cdot \mathcal{C}$$

In the case where one assumes that all the melt crystallizes at depth ("all-intrusive" scenario), the GEL height of water degassed ($h_{water,\ intrusive}$) is governed by the volatile retention capacity (X_{ret}):

$$(10)\quad h_{water,\ intrusive} = \max(0, X_{melt} - X_{ret}) \cdot h_{mafic} \cdot \mathcal{C}$$

The volatile retention capacity is controlled by the crystallization of hydrous minerals. Here, we defined X_{ret} as 0.20 wt.% H_2O, assuming that the intrusive rock consists of 10 wt.% of hornblende with a water concentration of 2 wt.%.

Global equivalent layer heights can be converted to a percentage of modern ocean volume, using a standard reference for the modern ocean GEL of 2700 m (*55*):

$$(11)\quad \text{Ocean Volume (\% Modern)} = \left(\frac{h_{\text{water}}}{2700}\right) \times 100$$

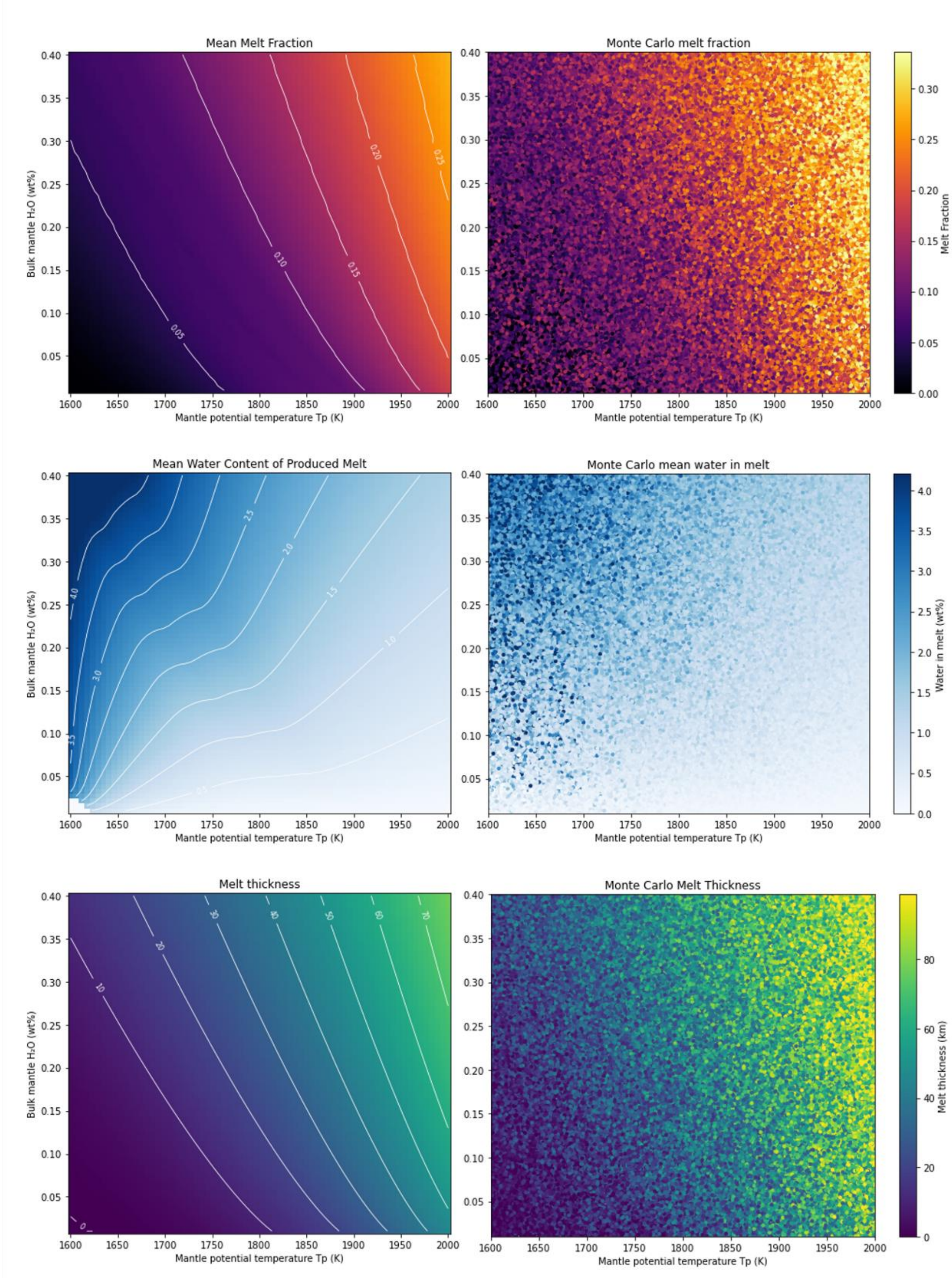

Fig. S1.

Monte Carlo simulation outputs. Left panels display melt fraction, water content of the melt and melt layer thickness (top to bottom) for fixed parameters (Table S1) and varying mantle potential temperature (Tp) and mantle source initial water content. Right panels display the result of 100,000 simulations with all parameters varying.

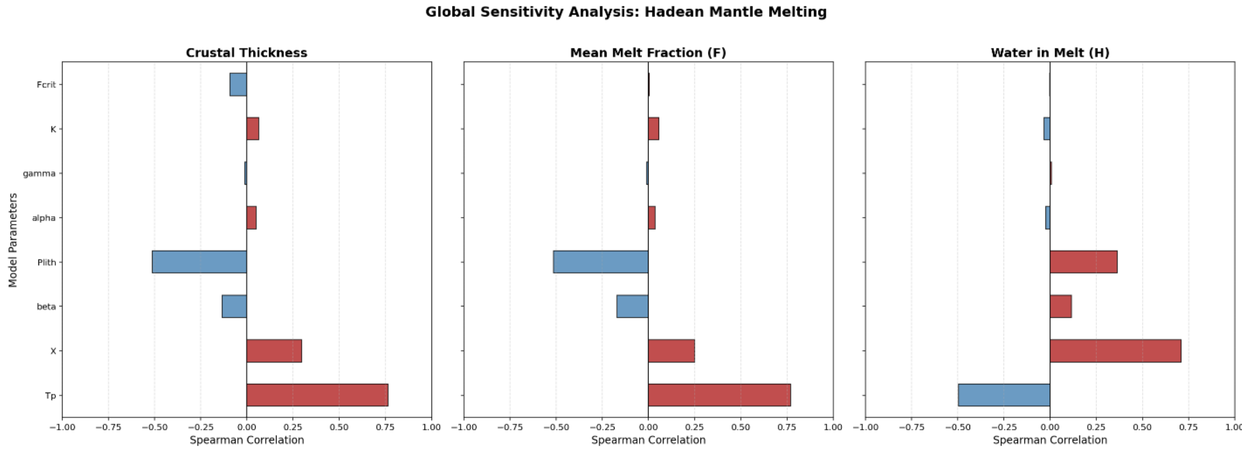

Fig. S2.

Global Sensitivity Analysis. The three panels display the correlation between the different parameters (Monte Carlo simulation inputs) and mafic layer thickness, melt fraction and water content of the melt (from left to right).

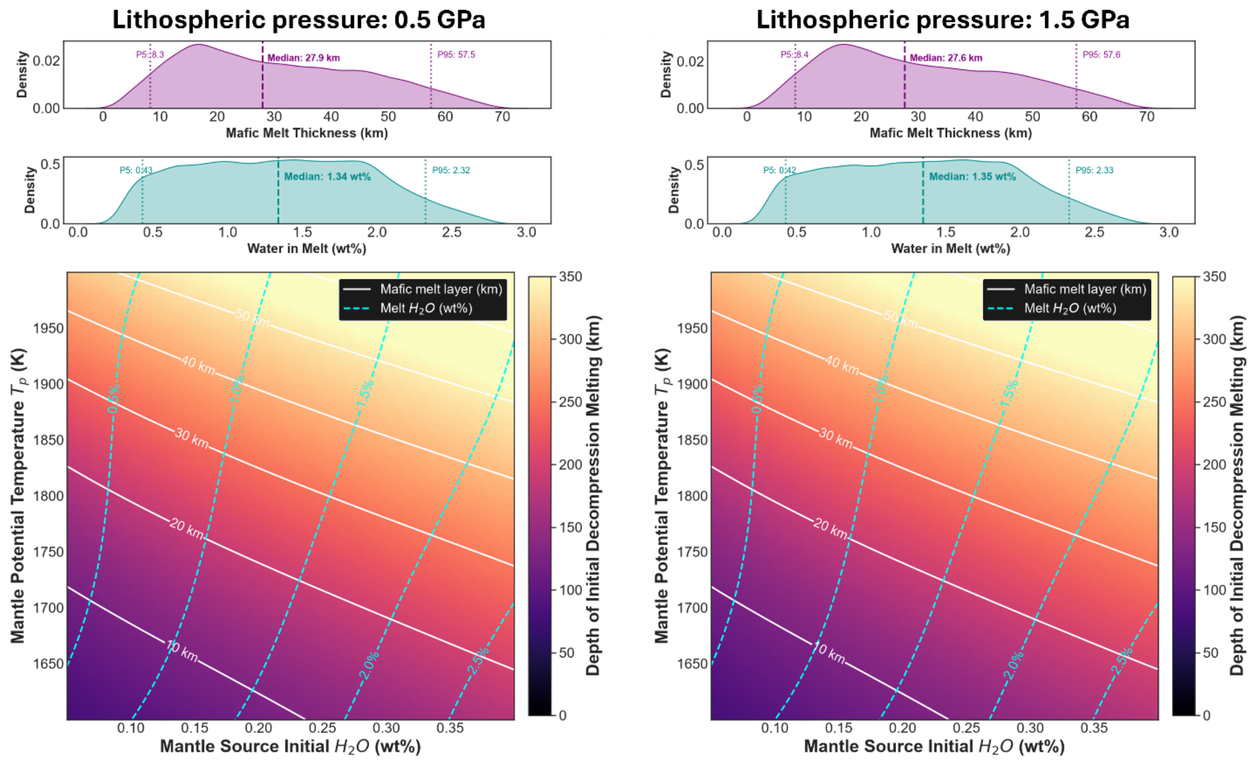

Fig. S3.

Monte Carlo simulation outputs for a lithospheric pressure of 0.5 and 1.5 GPa. Results are analog of Fig. 2 from the main text. Panels on the left side shows the predictive petrological abacus mapping partial melting behavior as a function of mantle source initial H_2O content (x-axis) and mantle potential temperature (Tp; y-axis), as well as Kernel density estimates (KDE) for the water concentration in the mantle melts and thickness of the primary crust, applying a lithospheric pressure of 0.5 GPa. Panels on the right side show the same for a lithospheric pressure of 1.5 GPa. The differences in the results between a 0.5 GPa and 1.5 GPa lithospheric pressure are small.

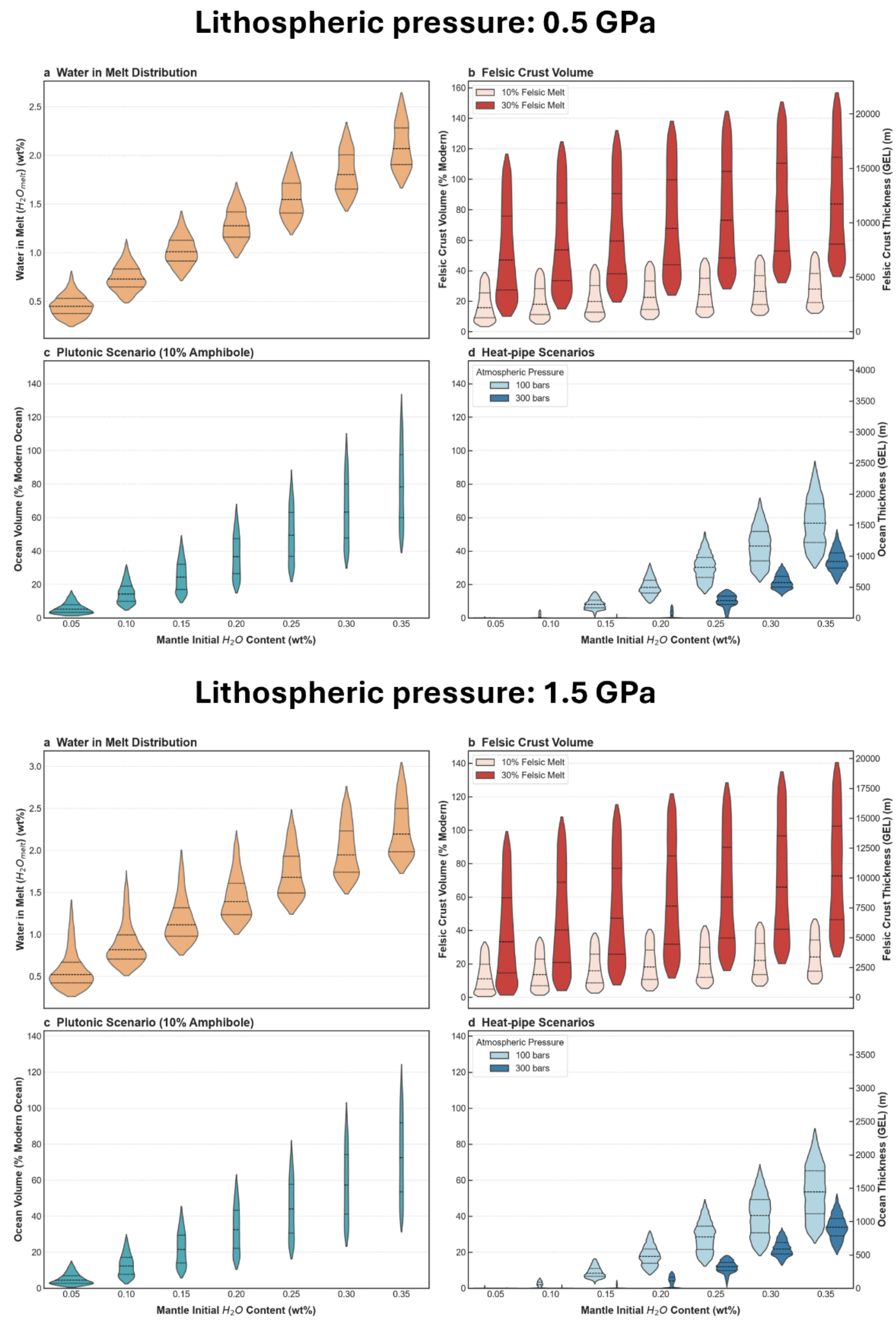

Fig. S4.

Water content of mafic melts, felsic crust production and ocean volumes as function of mantle initial water content for lithospheric pressure of 0.5 GPa and 1.5 GPa. Results are presented analog to Fig. 3 in the main text. Violin plots illustrate probability distributions from Monte Carlo simulations; dashed lines indicate the median and the 25th and 75th percentiles.

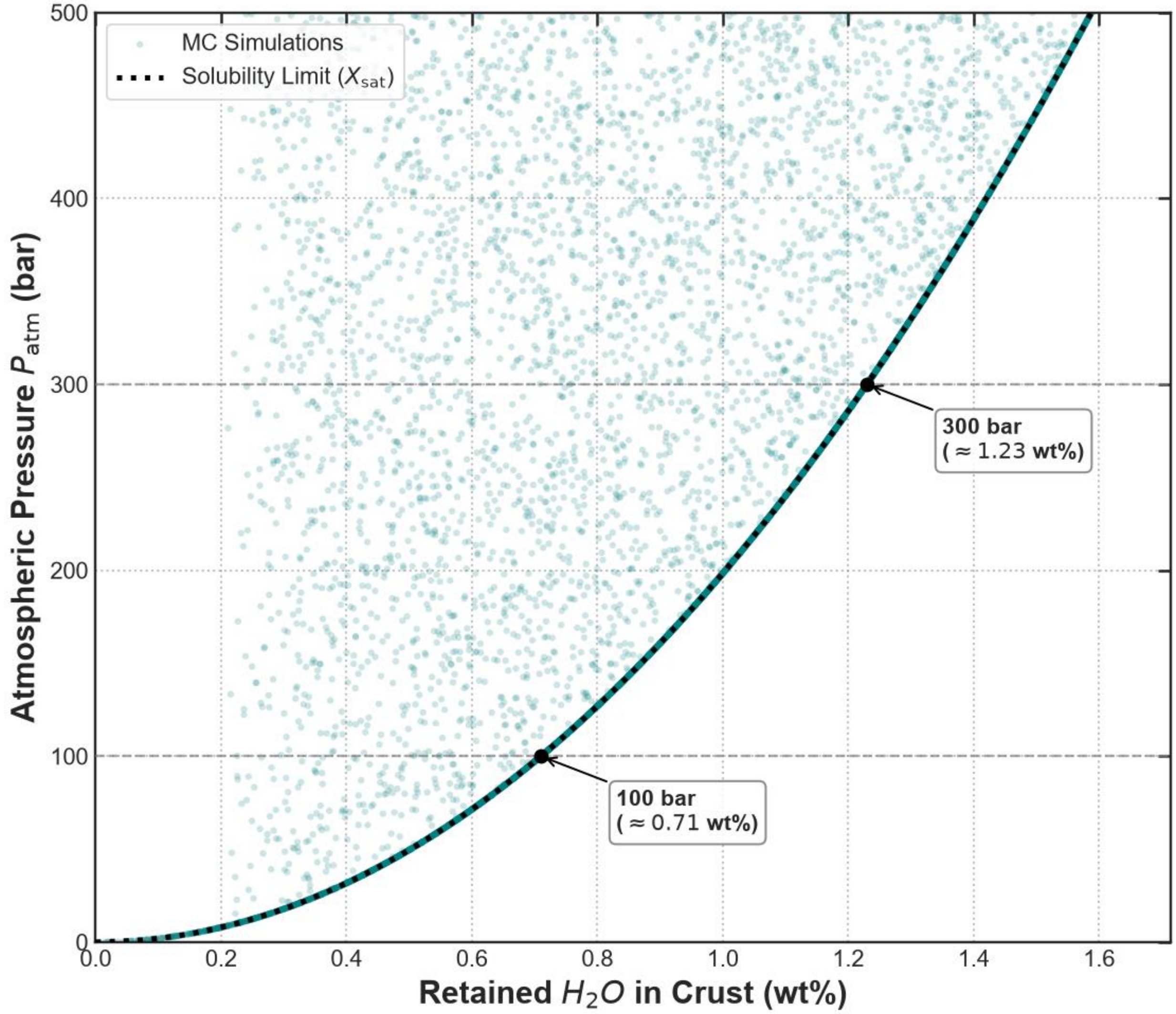

Fig. S5.

Crustal water retention as a function of atmospheric pressure (P_{atm}). Monte Carlo simulation illustrating retained H_2O in the crust under eruptive scenario (heat-pipe) across atmospheric pressure from 0 to 500 bar. Retained water is constrained by the pressure-dependent solubility limit (black dotted line), defined as the saturation threshold $X_{sat} = 0.071 \cdot \sqrt{P_{atm}}$ (*11*,*13*). Most simulations fall on the solubility limit because the simulated melt has a water content exceeding saturation threshold.

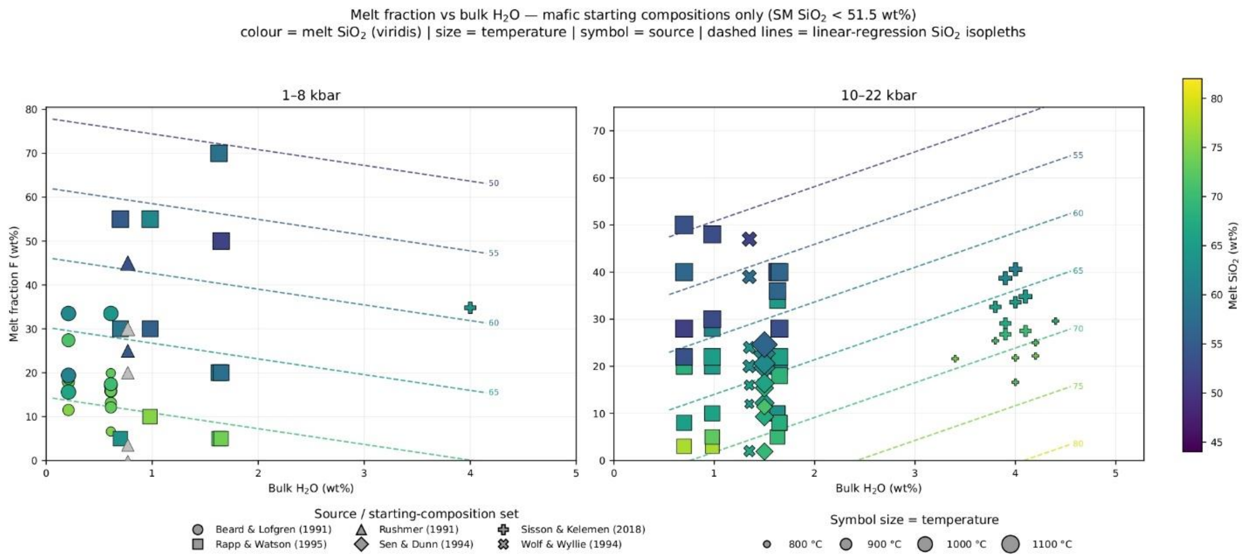

Fig. S6.

Compilation of experiments of partial melting of mafic lithologies. Panels show the relationship between melt fraction (F, wt.%) and bulk initial H_2O content (wt.%) for low-pressure (1 – 8 kbar) and high-pressure (10 – 22 kbar). Data are filtered for mafic starting compositions (SiO_2 < 51.5 wt.%). Color scale shows the melt SiO_2 content. Symbol scale displays the experimental temperature. Symbol shapes represent experimental data references. Dashed lines are linear regression contours representing constant melt SiO_2 concentrations.

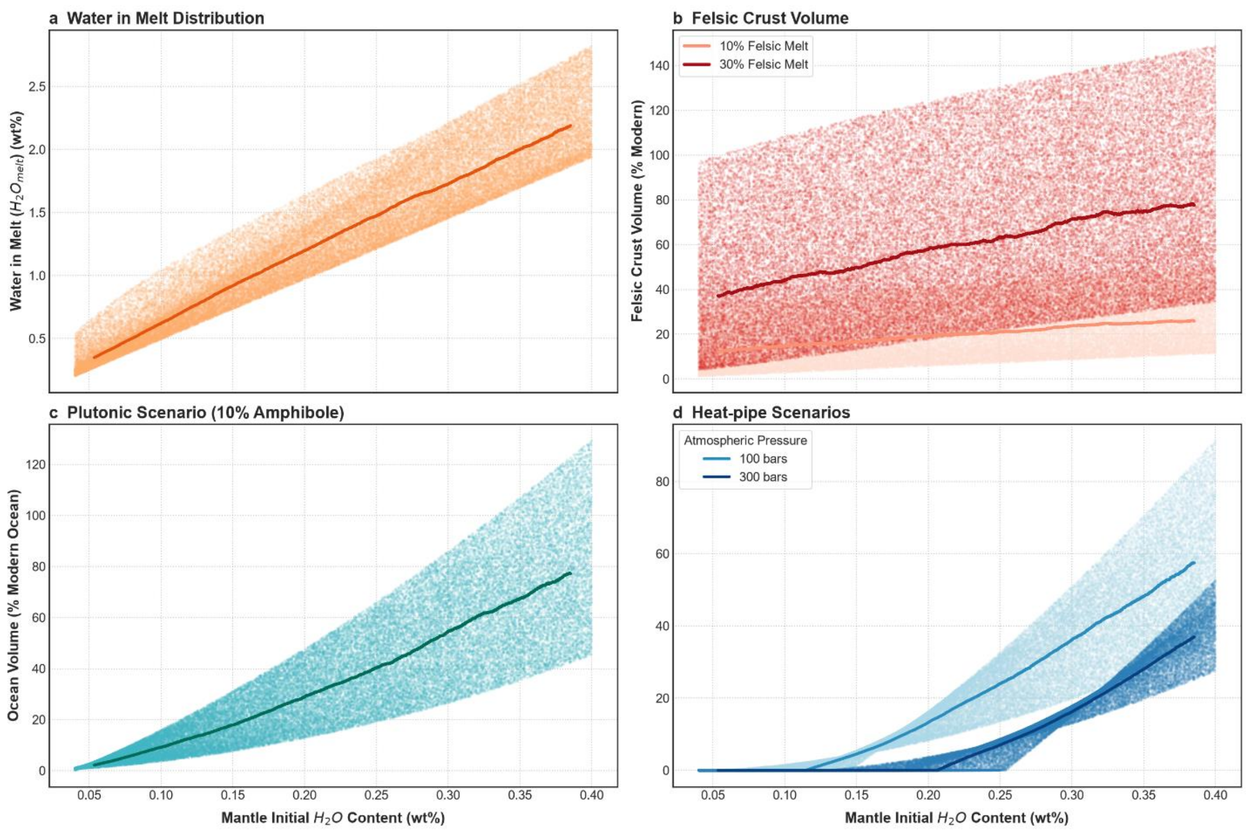

Fig. S7.

Individual Monte Carlo simulation outcomes. Scattered points show (a) dissolved water in the melt, (b) felsic crust volume, (c) ocean volume for plutonic scenario and (d) for heat-pipe scenario. Solid curves indicate the median of simulations.

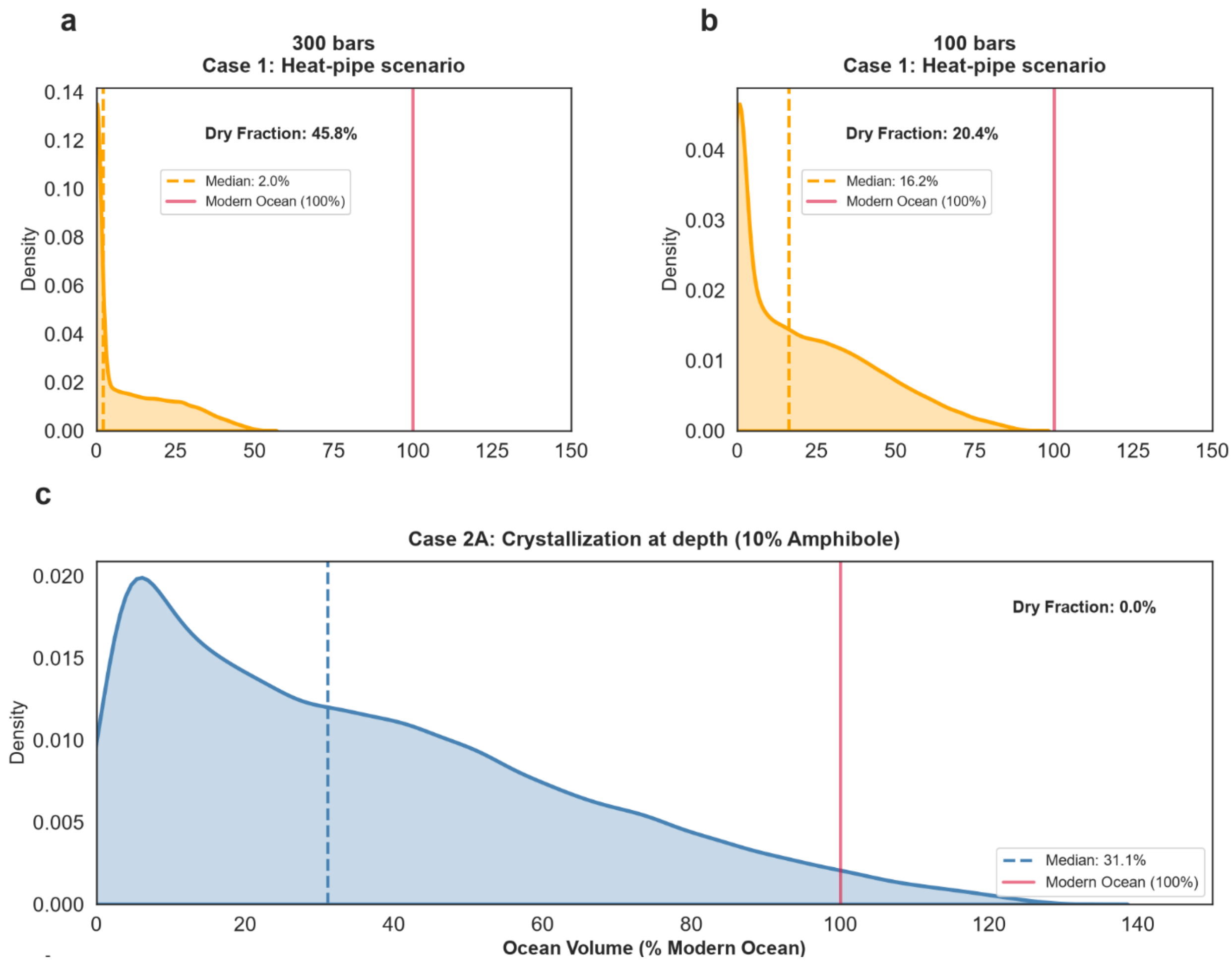

Fig. S8.

Distribution of ocean volume for different scenarios. Indicated are the volumes of surface waters shown as percent of modern ocean for (a) heat-pipe scenario at 300 bar atmospheric pressure, (b) heat-pipe scenario at 100 bar atmospheric pressure, (c) intrusive with 10 wt.% of crystallized hornblende.

Table S1.

Parameters sampled by Monte Carlo and fixed value chosen for further calculations.

Parameter	Unit	Sampling Range	Fixed value	References
Mantle water content	µg/g	500 - 4000		Elkins-Tanton, 2008; Marty, 2012; Peslier et al., 2017; Piani et al., 2020
Mantle potentail temperature	K	1600 - 2000		Herzberg et al., 2010; Korenaga, 2013; Andrault et al., 2018
Melting exponent β		1.2 - 1.7	1.5	Katz et al., 2003
Adiabatic gradient coefficient α	GPa-1	0.005 - 0.018	0.01	Katz et al., 2003
Depletion slope coefficient ϒ	K	200 - 400	300	Katz et al., 2003
Water partition coefficient		0.005 - 0.02	0.01	Aubaud et al., 2004; Hauri et al., 2006
Conductive Lid pressure	GPa	0.5 - 1.5	1	Marchi et al., 2026
Extraction threshold		0.01 - 0.05	0.03	Vogt et al., 2012